Formulation and Validation of Simulated Data for the Atmospheric Infrared Sounder (AIRS)

E. Fishbein, C.B. Farmer, S.L. Granger, D.T. Gregorich, M.R. Gunson, S.E. Hannon, M.D. Hofstadter, S.-Y. Lee, S.S Leroy and L.L. Strow

Abstract— **Models for synthesizing radiance measurements by the Atmospheric Infrared Sounder (AIRS) are described. Synthetics radiances have been generated for developing and testing data processing algorithms. The radiances are calculated from geophysical states derived from weather forecasts and climatology using the AIRS rapid transmission algorithms. The data contains horizontal variability at the spatial resolution of AIRS from the surface and cloud fields. This is needed to test retrieval algorithms under partially cloudy conditions. The surface variability is added using vegetation and IGBP surface type maps, while cloud variability is added randomly. The radiances are spectrally averaged to create High Resolution Infrared Sounder (HIRS) data and this is compared with actual HIRS2 data on the NOAA 14 satellite. The data are in agreement to 1-4 K, but the simulated data under represent high altitude equatorial cirrus clouds and have too much local variability. They agree in the mean to within 1-4 K and global standard deviation agree to better than 2 K. Simulated data have been a valuable tool for developing retrieval algorithms and studying error characteristics and will continue to do so after launch.**

Index Terms— **data simulation, atmospheric retrieval, algorithm development, satellite remote sensing, cloud scene modeling, HIRS**

I. Introduction

THE Atmospheric Infrared Sounder (AIRS) is a new generation nadir sounder that will measure high-spectral, high-spatial thermal infrared (IR) radiances globally from low-earth polar orbit. These measurements will provide new information on the thermal and compositional structure of the earth's atmosphere and surface. In doing so, state variables, e.g. atmospheric temperature and composition will be estimated using complex retrieval algorithms. The AIRS science team has created simulated radiances to prepare these algorithms for launch. The data described here have been used to develop retrieval algorithms, [1] test calibration algorithms [2,3,4] and develop data processing systems [5].

Creating this data has proven to be a difficult task. The development team wanted data that would realistically test the algorithms and permit valid error characterization of products. However, time constraints necessitated a simple model early in the development cycle that has continually been updated as required by the algorithm development team. We discovered that simulated data would continue to be used for algorithm testing after launch, and that interpreting test results would depends on an understanding of the formalism and basis of the data simulation. We noticed also that while every flight instrument team develops simulated data, very few document or validate it in the refereed literature. This last activity is extremely important because unrealistic data can lead to flawed algorithms. However doing so with an instrument, such as AIRS, is difficult because data from less sophisticated instruments do not contain as much information as will be provided by AIRS. We demonstrate how data from the High Resolution Infrared Sounder was used to validate our simulated data.

AIRS is a major advance for this kind of spaceborne instrument with characteristics unlike any instrument that has flown before. We realized that simulated data could not be created by manipulating similar radiance data sets, and simulated radiance data would not be useful unless we knew the corresponding geophysical state. Therefore we took the approach of generating realistic geophysical states and using a radiance forward model to generate the simulated radiance data. This provided radiance data and corresponding geophysical states. The states could be compared with retrieval products to assess product errors, but the assessments would be dependent on the accuracy of the forward model. For reasons such as this, the simulated data, while a valuable tool for error characterization but, is also an incomplete one.

The kinds of data that are used to construct geophysical states depends on the goals and design of the AIRS measurement system. The term "measurement system" refers to the suite of instruments and calibration and analysis software that as a combined system produce the AIRS products. The goals of the AIRS measurement system are to produce profiles of air temperature and water vapor mixing ratio with near radiosonde (in situ) quality. This is defined to mean temperature profiles with 1 K root mean square (RMS) accuracy in 1 km thick layers in the troposphere and humidity profiles with 10% accuracy in the troposphere [6]. While these are the primary goals of the investigation, AIRS radiances will also provide measurements of other variables such as cloud and surface properties and atmospheric trace gases such as carbon dioxide and methane.

The AIRS measurement system include AIRS and two microwave radiometers, the Advanced Microwave Sounder (AMSU) and the Brazilian Humidity Sounder (HSB). AMSU is a copy of a NOAA operational sounder currently on two NOAA Polar Orbiting Environmental Satellites (POES), while HSB is derived from AMSU-B, also operating on two POES satellites. Descriptions of AIRS, AMSU, HSB and the Aqua platform and orbit characteristics can be found in References [7,8,9,10,11]. Synthetic data has been derived for all three instruments, but

E. Fishbein, C.B. Farmer, S.L. Granger D.T. Gregorich, M.R. Gunson, M.D. Hofstadter, S.-Y. Lee and S.S Leroy are with the Jet Propulsion Laboratory, California Institute of Technology, Pasadena, CA 91109. E-mail Evan.Fishbein@jpl.nasa.gov

S.E. Hannon and L.L. Strow are with the Dept. of Physics, University of Maryland, Baltimore County, Baltimore, MD 21205

owing to the uniqueness of AIRS, and the special properties of its measurements, only the AIRS synthetic measurements will be described in this paper.

The instruments will be mounted on NASA's Aqua satellite. Aqua will be in a 705 km altitude polar orbit, maintained with a 1:30 PM local-time ascending equator-crossing. The orbit will conform to the Worldwide Reference System with a 233 orbit (16 day) repeat cycle. AIRS cross-track-scans three scan lines every 8 seconds. Each scan line contains 90 footprints. The field of view (FOV) is 1.1°, producing an approximately 14 km diameter footprint at nadir. The FOV's centers in adjacent scanlines are separated by approximately 16 km. AIRS is a 2378 channel grating spectrometer with three major pass bands, 650–1140 cm^{-1}, 1215–1610 cm^{-1} and 2180–2665 cm^{-1}.

The other main component of the measurement system are the retrieval algorithms. Retrieval algorithms typically solve complicated often under-constrained mathematical problems [12],[12], which are made solvable by applying constraints and smoothing conditions. Assimilation is an advanced form of this conditioning which makes use of an atmospheric circulation model. The AIRS retrievals algorithms are designed to demonstrate the capabilities of hyperspectral sounding and are not based on this, but it is expected that AIRS data will be assimilated at a latter date. A description of the AIRS retrieval algorithms can be found in Ref. [1].Briefly, the retrieval algorithms estimate an optimal geophysical solution by fitting model radiances to observations and minimizing the normalized RMS residual. Simulated data provides both radiances and a perfect assessment of the geophysical state (hereafter referred to as "truth"). The retrieval problem does not guarantee that the optimal solution is also a reasonably meteorological one. However, having both radiances and geophysical states allows us to specify constraints which produce both an optimal and reasonable solution. How applicable these constraints are depends on the degree to which the simulated states and radiances are representative of real observations.

The retrieval algorithms are formulated to operate on cloud-free radiances. Intrinsic to the AIRS measurement system design philosophy is a concept called "cloud clearing," which states that clear radiances can be estimated from a set of near-located cloudy radiances without a full retrieval. Intrinsic to cloud clearing is an assumed spatial scale separation between cloud variability and other sources of variability. In particular, over distances of around 50 km, most of the variability in 15 km areas arises from variation in cloud amount while surface properties and profile quantities are mostly constant. We refer to variability on this length scale as "local." With this in mind, the scans and FOV's of AIRS, HSB and AMSU are designed to lead to an arrangement of footprints in a 'golfball" pattern shown in Figure 1. The retrieval system operates on groups of 19 FOVs (9 AIRS, 9 HSB and 1 AMSU) referred to as a retrieval set, and retrieves one set of atmospheric profile and surface quantities per group, but one cloud fraction for two cloud layers for each AIRS footprint.

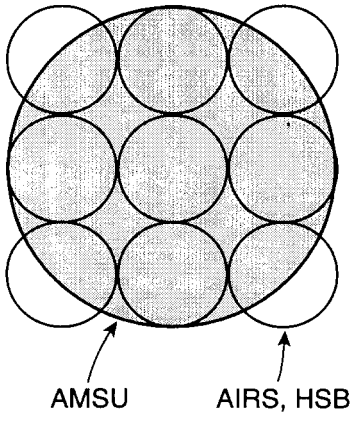

Fig. 1. Arrangement of AIRS, HSB and AMSU footprints

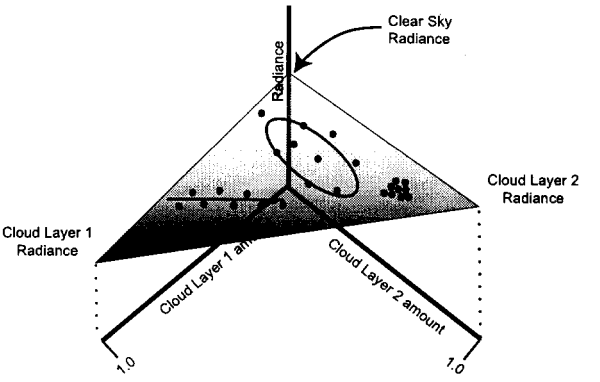

Fig. 2. Cloud Clearing Procedure

The cloud clearing procedure [1,13,14] is relatively straightforward for many kinds of clouds, e.g. gray or opaque clouds in otherwise optically transparent channels. The observed radiances for footprints derived from the same state but varying cloud amounts are linear combinations of the surface radiance and the emission from the clouds. For the case of multiple cloud levels, the mapping of cloud amount (fraction) onto outgoing radiance defines a hyperplane. Figure 2 illustrates the plane in radiance-cloud fraction space. The two horizontal axes are cloud amount and the vertical axis is outgoing radiance. The outgoing radiance is the linear combination of radiance from the surface, and from the two cloud layers weighted by the amounts of viewed surface and cloud. Once the plane is determined, the radiance when the cloud fractions are zero is known. The problem is to determine the plane from nine cloud amounts-radiance measurements. There are three possible measurement scenarios illustrated in Figure 2. The first is when the measurements are distributed over a plane, i.e. the covariance matrix has two unique axes. The second is when the measurements lie on a line, i.e. the radiance covariance matrix has one unique axis, and the last is when all measurements are at one point, i.e. the covariance matrix is zero. In all but the first case, the plane is not constrained by the measurements and the cloud clearing problem is ill conditioned. The cloud clearing problem is further complicated because the cloud fractions are not directly measured, but are retrieved from infrared and microwave radiances together. Later under cloud models, we will discuss a parameter for characterizing the stability of cloud clearing.

Since the cloud-clearing algorithms are based on assump-

tions of horizontal variability, the simulations must have realistic correlations over 50 km. Global data sets typically resolve scales larger than 50 km. This means that the assumptions of cloud clearing could not be tested globally with available data. We therefore created ad hoc models for sub 50 km variability for these simulations.

II. Formalism of the Simulations

A. Radiance Generation

Radiances are generated using a 1-dimensional rapid transmission algorithm (RTA) described in [15] with an enhancement for two layers of optically thick clouds. The AIRS RTA parameterizes channel averaged transmittances across 100 atmospheric layers in terms of predictors which includes products and powers of the local zenith angle, layer mean temperature and layer amounts of water vapor, ozone, methane and carbon monoxide. Variability of transmittance from variations in carbon dioxide is also included through a scaling in column-mean carbon dioxide mixing ratio.

Clouds, like the surface, are treated as gray emitters and Lambertian reflectors. Clouds radiate with a temperature of the ambient air at the cloud-top. The outgoing radiance is a linear combination of clear sky and cloudy radiances weighted by the cloud fractions. The cloud fraction of the lower layer is the amount of cloud unobscured by the upper cloud layer when looking along the zenith angle; the angle dependence resulting from cloud thickness is not included. The cloud-top to space transmittances are interpolated from the clear sky transmittances and the incoming transmittance are approximated by the outgoing ones using a regression based correction factor [15]. The correction factors are derived from transmittance to the surface and are less accurate when applied at cloud-top pressures.

The reflected solar component of the radiances, important in the high wavenumber channels, is not accurately calculated using the approximate transmittances and reflectivities of this model. In particular the down welling thermal radiance and the incoming solar radiance are reflected off the clouds and surface with the same reflectivities; sun glint is not modeled by these approximations.

The radiative transfer algorithms used in the retrieval and simulated data are equivalent and therefore errors and approximations are self consistent (closed). Although each footprint sees an ensemble of states, one radiative calculation is performed per footprint, using average surface and atmospheric conditions.

The set of parameters needed to generate radiances include satellite attitude and ephemeris, solar ephemeris, instrument view geometry and geophysical data. All parameters derived from digital geography models (DGM) and satellite and solar ephemeri, e.g. location of footprint, mean elevation and land fraction, and position of the sun and satellite relative to the center of the footprint are calculated using the EOS scientific data processing toolkit [16].Geophysical parameters include atmospheric profiles, cloud properties and surface properties, and are listed in Table I. These are derived from operational global forecasts and climatologies. Cloud amounts, emissivities and reflectivities; and surface emissivities and reflectivities with the required local variability are generated using ad hoc models described later.

Quantity	Units
Surface pressure	hPa
Surface skin temperature	Kelvin
IR Surface Emissivities	0–1.0
IR Surface Reflectivities	0–1.0
Carbon dioxide volume mixing ratio	ppmv
Air temperature	Kelvin
Water vapor volume mixing ratio	ppmv
Ozone volume mixing ratio	ppmv
Liquid water volume mixing ratio	ppmv
Carbon monoxide volume mixing ratio	ppmv
Methane volume mixing ratio	ppmv
Viewed cloudiness	0-1.0
Cloud-top pressure	hPa
Cloud emissivities	0–1.0
Cloud reflectivities	0–1.0

TABLE I
GEOPHYSICAL STATE PARAMETERS

B. Geophysical Parameter Modeling

The geophysical state at each footprint is interpolated in space and time from gridded synoptic and monthly climatological data. Methane and carbon monoxide profiles are global time-independent climatologies. For all other fields, the grids are first interpolated to the footprint time using either forecasts derived from a single analysis, or climatologies from bracketing months; the climatologies are assumed to be synoptic at 1200 UT on the fifteenth of the month. For example, a footprint at 0430 UT in the second half of December would use the 3 and 6 hour forecasts from a 00 UT run and climatologies from December and January. A linear or bilinear interpolation is applied within latitude bins or grid boxes. In the vertical, profiles are interpolated, linearly in log pressure, to a standard 101 level grid described in [15].

1) Data Sources: Geophysical data are obtained from the NCEP global aviation forecasts and Advanced Very High Resolution Radiometer (AVHRR) composite Normalized Differential Vegetation Index (NDVI) imagery. Climatologies are used in regions of the atmosphere not contained in the forecast; these include the Upper Atmosphere Research Satellite (UARS) climatology, the Harvard tropospheric ozone climatology and the ATMOS methane climatology (the average of profiles obtained by the ATMOS investigation [17]. The carbon monoxide profile is from the U.S. standard atmosphere. Vertical-mean carbon dioxide mixing ratio is obtained from a simple empirical model described later.

The U.S. National Center for Environmental Prediction (NCEP) produces global operational aviation analyses and forecasts (GBLAV) four times daily at 0 UT , 6 UT, 12 UT and 18 UT; outputting 3 hour forecasts at least three days forward.

The products are mostly synoptic fields on 1° longitude by 1° latitude grids. We use the surface fields of wind, pressure, geopotential height and skin temperature; atmospheric profiles of air temperature, relative humidity and ozone mass mixing ratio, and the three hour average fields of low, middle and high cloudiness and the cloud-top and cloud-base pressure from the forecasts. Temperature, relative humidity and ozone profiles are parameterized on 26, 21 and 6 levels from 1000 hPa (ozone from 100 hPa) to 10 hPa (relative humidity to 100 hPa). Land skin temperature is the upper level of a two layer soil model that includes radiative and conductive heat transport, soil moisture transport and evaporation Reference [18]. Sea surface temperature is the temperature at 1 m depth from a daily analysis of AVHRR and buoy data; no correction has been made for the difference from skin temperature. There are 4 kinds of stratiform clouds (high, middle, low and planetary boundary layer) and cumulus clouds from the convective scheme. The amounts, heights and radiative properties of stratiform clouds are derived from statistical relations between cloud amount and relative humidity binned by location and height [19].The cumulus convective scheme is described in Reference [20],and the cumulus cloud model is described in Reference [19].Further details of the aviation forecast model can be found in References [21,21,23].

The UARS climatology was derived from the Middle Atmosphere Program climatology prior to the launch of the Upper Atmosphere Research Satellite in September 1991. It contains monthly zonally-averaged means of temperature and 18 species including, H_2O, O_3, CH_4 and CO. The model has 10° resolution with grid points at -80° S, -70° S.... We have used the temperature and ozone climatologies above 10 hPa and the water climatology above 100 hpa.

The Harvard climatology is described in Reference [24]and contains monthly tropospheric ozone values from pole to pole in 5° longitude bins and 4° latitude bins on 13 pressure levels from 1000 hPa to 100 hPa. This climatology is used to complete the ozone profile below 100 hPa.

NDVI is a scaled color index and measures the amount of chlorophyll in a pixel. The imagery are 10-day cloud-free composites derived from AVHRR data. Cloud-free pixels are mapped onto an Interrupted Goode Homolosine projection (averaged if multiple pixels exist) using a procedure described in Reference [25,26]. We have used an 8 km product from the NOAA/NASA Pathfinder project produced from July 1981 through September 2001 and a 1 km product produced by the USGS Eros Data Center from April 1992 through May 1996. The amount of the globe that has useful NDVI information depends on season and equator crossing time of sun synchronous satellites. The most complete NDVI imagery are taken during equinox by satellites in noon equator-crossing orbits; the worse are at solstice by satellites in 600PM equator crossing orbits.

2) Profile Quantities: Profiles are constructed from several sources covering different levels of the atmosphere. One of the problems when profiles are from different sources are joined together is maintaining the correlations observed in the atmosphere; this is especially true when profiles are not consistent at common levels. We have addressed this issue by implementing a smoothing procedure where profiles are extrapolated over common levels and then combines them using a smoothing function $f(P)$. The combined profile $X(P)$is

$$X(p) = f(P)X_l(P) + (1 - f(P)X_u(P)$$

where P is pressure, X_l is the lower profile and X_u is the upper profile. The smoothing function is

$$f(P) = \frac{1}{2}\left\{1 - \tanh\left[\frac{\log_{10}(P/P^*)}{H}\tanh^{-1}0.9\right]\right\}.$$

where P^* is the tie-point pressure where each profile contributes equally to the output and H is the smoothing width. Profiles were joined at 10 hPa and 100 hPa using smoothing widths of 1 and 0.5 respectively. These widths are smaller than the correlation widths we have calculated for the aviation forecast products.

Water profiles are constructed using two approaches. One, discussed above, combines the UARS climatology with the forecast relative humidity at 100 hPa. The profiles are interpolated in units of specific humidity (i.e. water vapor wet mass mixing ratio). Specific and relative humidities S and Rh are related by

$$S = \frac{0.01RS_s}{1 - (1 - 0.01Rh)S_s}$$

where S_s is the saturation specific humidity, provided by a function fit to the Smithsonian Meteorological Tables [27].A second approach employs power law extrapolation of the forecast specific humidity in pressure.

3) Carbon Dioxide: Carbon dioxide amount is included in the simulation using a model that has temporal and latitude dependence. The model is based on ground observations and includes a positive trend, seasonal variability and a surface source whose rate is slow compared to transport. The trend (X^{trend}) and seasonal (X^{seasonal}) terms are:

$$\begin{aligned} X^{\text{trend}}_{CO_2}(\theta) &= 331 \times 1.0041^{(T-1976)} \\ X^{\text{seasonal}}_{CO_2}(\theta, P) &= [7.9\,\text{erf}\,(2\sin\theta) + 6.4] \\ &\quad \sin(2\pi T - \pi/6)\ (P_0/P)^{0.4222}, \end{aligned}$$

where mixing ratios X are in ppmv, time T is in common years (from 0 CE), θ is the latitude in radians and pressure P is in hPa. The reference pressure P_0 is 1000 hPa and the exponent is the ratio of the CO_2 vertical mixing length (3.3 km) to the scale height 7.817 km. Variability is largest in late winter and smallest in late fall. The vertical, pressure-weighted average mixing ratio is

$$\bar{X}_{CO_2} = X^{\text{trend}}_{CO_2}(\theta) + (0.4222/1.4222)\, X^{\text{seasonal}}_{CO_2}(\theta, P_0)$$

The model is based on observations at ground stations at Mauna Loa and the South Pole and its transport (see Reference [28]).Figure 3 compares the model concentrations at the Mauna Loa observatory to observed monthly means. The model agrees well with the observations, although the minimum in early November is about 10 ppmv lower in the model and occurs 1 month later. The amount of spatial variability is shown in Figure 3 by the difference between values at the poles. The maximum amount of variability is about 4%, but is only 2% in late December and zero in late January and July.

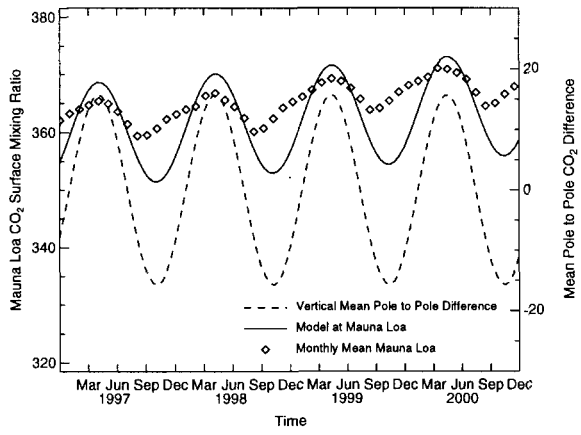

Fig. 3. CO_2 Surface Mixing Ratio Time Series

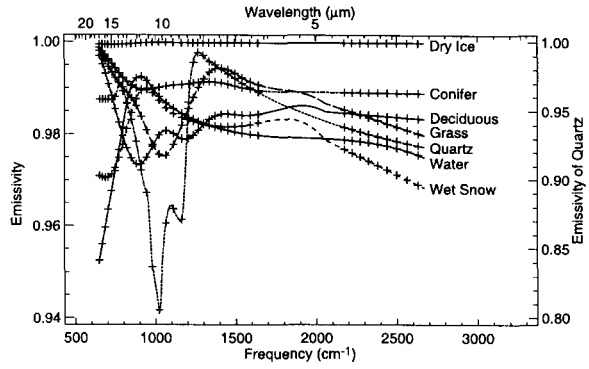

Fig. 4. Infrared Spectral Emissivities of Land Surface Materials

4) Surface Properties: Skin temperature, surface pressure and geopotential height are interpolated from the forecast. Surface geopotential height is converted to elevation and surface pressure is corrected for local elevation. Mean elevation and land fraction are calculated from approximately 100 samples of a 30″ DGM. The surface pressure correction adjusts the forecast surface pressure for the differences in elevation between the interpolated forecast elevation and the elevation from the DGM. The correction assumes a dry adiabatic surface layer (see Reference [29]).The skin temperature is the interpolated value from the forecast and is not corrected for local variations in surface properties such as soil moisture or coast line crossings.

Surface emissivities and reflectivities are represented as a piecewise linear function in frequency, specified at 39 hinge points (the hinge points are indicated by '+' in Figure 4). Land is a Lambertian emitter (emissivity is independent of emission angle) and both land and water are Lambertian reflectors. The emissivity of water depends on surface temperature, emission angle, salinity and surface wind speed and is based on theoretical calculations described in References [30,31,32,33]. Surface wind speed is obtained from the forecast, while salinity is fixed at 34.3‰.

Land emissivity is considerably more variable and depends on soil composition, vegetation type, amount of vegetation and snow and ice coverage, but the single largest source of emissivity variability is the vegetation density. The land emissivity model is based on a scheme described in Reference [34]where land is composed of a mixture of ground and vegetation, but the amount of vegetation varies according to NDVI. A vegetation model is adopted that relates vegetation coverage f_v linearly to NDVI. Vegetation fraction is zero when NDVI is less than 0.1 and 1 when NDVI is greater than 0.6. This relation is consistent with the observed range of NDVI reported in Reference [35].NDVI is sampled from the AVHRR image at the center of the footprint without any averaging over the area of the footprint to reduce computations. The model assumes that the amount of vegetation observed at visible frequencies and correlated with chlorophyll amount, is equal to the amount of vegetation observed in the thermal IR and correlated with water amount.

The types of ground and vegetation are estimated from the 17 International Geosphere Biosphere Programme (IGBP) land use classes [36].The number of land classes has been simplified to 9: 1) deciduous forest, 2) evergreen forests, 3) mixed deciduous and evergreen forests, 4) grasslands, 5) marsh, 6) urban landscape, 7) mosaic, 8) tundra, and 9) ice. There are three vegetation materials: grass, conifer and deciduous, and five ground materials: water, soil/rock, wet snow, dry ice and black material (e.g. asphalt/concrete). Land can contain a mixture of the three vegetation types and one ground material. Although the amount of vegetation is specified by NDVI, in those land classes containing more than one vegetation type, the relative amount of each vegetation type is random (i.e. derived from a uniform random variate). Soil and rock emissivities are highly dependent on composition, but typically have a strong absorption feature (restrahlen band) in the 8 to 10μm spectral region [37].Soils composition is approximated by pure quartz sand which has one of the strongest absorption features. The forests (first three classes) are mixtures of forest over quartz sand, grassland, a mixture of grass over quartz sand; marsh, a mixture of grass and water; and urban, a mixture of grass and black material. Mosaic is a mixture of all three vegetation types over quartz sand; tundra, a mixture of conifer forest over wet snow; and ice is grass over dry ice. Footprints can contain a mixture of land and water as specified by the land fraction.

The spectral emissivities of water, dry ice, conifer foliage, deciduous foliage, grass, quartz sand, water and wet snow are shown in Figure 4; black material is unity and is not shown. The quartz emissivity is from Reference [38]and is plotted on the right. The remaining models (excluding water) are interpolated from Reference [34].The water emissivity is shown for nadir viewing of a calm (zero wind) surface. With this model, most of the variability occurs between 800 and 1300 cm^{-1} and mostly from quartz sand. Vegetation provides some variability although much smaller. Emissivities at frequencies between 2000 and 3000 cm^{-1} are extrapolated from longer wavelength and are less reliable.

5) Cloud Properties: Cloud parameters have proven to be the most difficult field to simulate reliably, owing to their dependence on instrument scan pattern and instrument FOV. Moreover, since these conditions cannot be replicated with existing measurements or synthesized from other data, we have adopted simple models of cloud variability based on reasonable assumptions described below. Several approaches were consid-

ered including, generating fractal cloud distributions (see Reference [39]) or running a dynamical high resolution weather or convection model (see Reference [40]). We deemed either procedure impractical and ultimately settled on applying random perturbations to cloud properties interpolated from forecast.

Cloud models have been developed using three different perturbation schemes. In all cases only the cloud amounts were perturbed. All models use the two highest stratiform cloud layers from the forecast; this reduces the total cloudiness slightly, but includes those layers producing the largest radiance signatures. The first model applies a 30% Gaussian random perturbation to each amount. Perturbations are regenerated whenever the perturbed amount is greater than one or less than zero. The clouds are assumed to be small and spatially uncorrelated; therefore the amount of the lower layer seen from above is $\acute{f}_l^{Viewed} = (1 - \acute{f}_u)\acute{f}_l$. $\acute{f}_u$ and $\acute{f}_l$ are the perturbed cloud amounts in the upper and lower layers. Note that because the clouds are randomly distributed in the two layers, the viewed cloud amount in the lower layer is anti-correlated with the upper; this gives rise to singular cloud clearing situations as exemplified in Figure 2.

A second model was introduced to reduce the number of singular cloud fields found in Model 1. In the second model the amounts are scaled by a normalized uniformly-distributed random variable. Mean cloud amounts and heights are evaluated for the nine footprints in a retrieval set. The perturbed amounts in the upper or lower layer are

$$\acute{f}_{\{u,l\}} = \frac{n_{\{u,l\}}}{\bar{n}_{\{u,l\}}} f_{\{u,l\}} ,$$

where $n_{\{u,l\}}$ are numbers from a uniform random variable and $\bar{n}_{\{u,l\}}$ are averages over retrieval set (9 footprints) in each layer. Subscripts indicate upper or lower layers and un-accented amounts are the interpolated forecast amounts averaged over retrieval sets. Whenever the perturbed amount exceeds one, it is reduced by the mean amount $\bar{n}_{\{u,l\}}$. The viewed amount in the lower layer is reduced by the forecast amount in the upper level, $\acute{f}_l^{Viewed} = (1 - f_u)\acute{f}_l$, and not the perturbed amount. This introduces some correlation between the perturbations, but not the total cloud amounts.

The third model applies perturbations to cloud amount using a relation between mean cloud amount and cloud amount variability derived from Monte-Carlo simulation. The Monte Carlo simulation populated a plane with randomly distributed non-overlapping clouds until a mean cloud amount was obtained. AIRS footprints were next randomly overlain on the cloud field and cloud amount in each footprint was determined. Lastly the density function was estimated. This was repeated as a function of mean cloud amount. AIRS footprints and clouds were approximated by circles with effective radi ($r_{\text{eff}} = \sqrt{\text{Area}/\pi}$), and the problem was recast in terms of one parameter, the ratio of cloud and footprint radii. Figure 5 shows cloud amount density for 25% average cloudiness for a 15 km AIRS footprint and 3 km and 7.5 km clouds. Distributions of bounded random variables often obey beta distributions [41],The smooth curves in Figure 5 are beta distributions fit to the observed densities and are in very good agreement. We therfore fit beta distributions to the observed density functions and constructed a relation of standard deviation versus mean. The width of the density functions rapidly decreases as cloud radius becomes small relative to the footprint radius; this is the limit where the footprint samples the average cloud field. Figure 6 shows the dependence of cloud fraction standard deviation on mean cloud fraction for an effective cloud radius of 7.5 km. We found that the density functions became unlike a beta distribution as the mean cloud amount approached 0.5. This arose because higher mean cloud amounts were possible only when the clouds became organized. In fact, mean cloud amount for non overlapping circular cloud can never be greater than ($\pi/4 = 0.785$) and this occurs only when the clouds are arrange in closest packing. To simulate higher mean cloud amounts, we reverse the simulation by randomly distributing non overlapping holes. It became clear that the minimum in variability near 0.5 is an artifact of the cloud size and shape distributions. We there fire adopted a cloud amount variability model shown by the solid line in Figure 6.

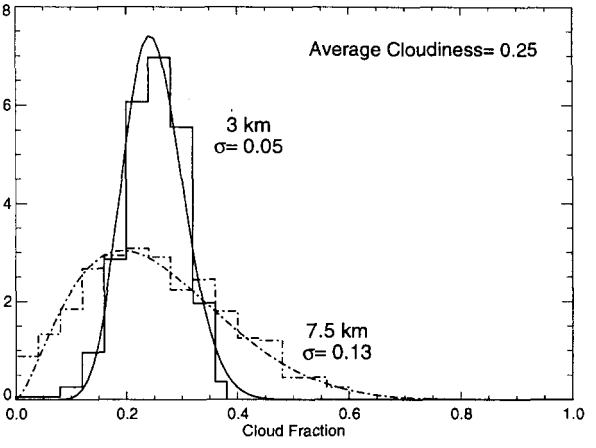

Fig. 5. Cloudiness Distributions from Monte Carlo Simulation

The third cloud model assumes a fixed ratio of AIRS footprint effective radius which is adjustable. However we present results only when the footprint radius to cloud effective radius is 2. The cloud amounts are random numbers from a beta random variate with a mean cloud amount obtained from forecast, as in the second model, and a standard deviation from Figure 6. The

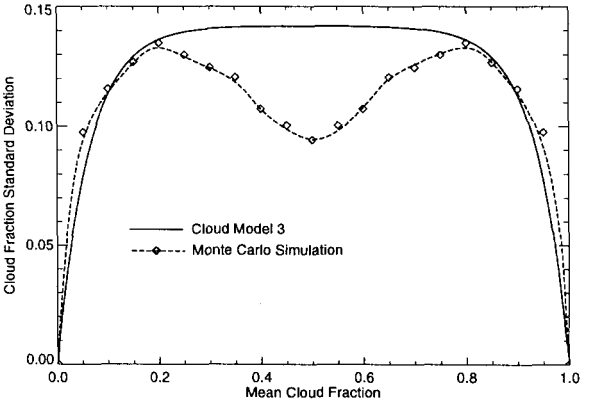

Fig. 6. Monte Carlo Simulated Cloudiness Variability

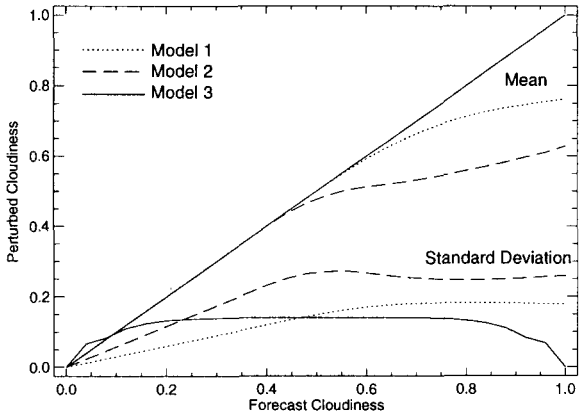

Fig. 7. Cloud Model Statistics

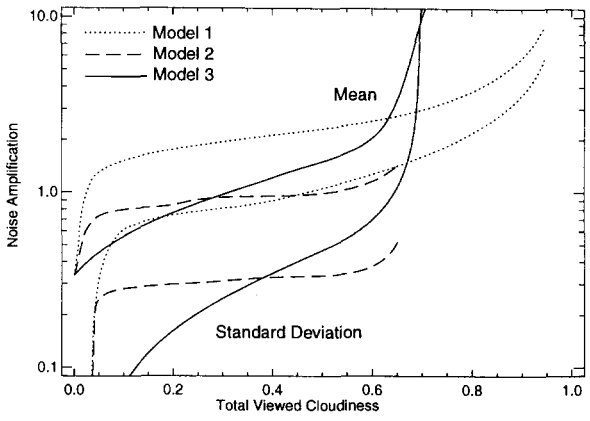

Fig. 8. Cloud Noise Amplification Factor

viewed lower cloud layer is the same as in model 1 as described above.

An ensemble of perturbed cloud fields were generated as functions of forecast cloud amount for the three models. Figure 7 show the mean and standard deviation of the perturbed cloudiness as a function of forecasted total cloud amount (total forecasted cloud amount assumes small uncorrelated clouds, i.e. $f_u + (1 - f_u)f_l$). The third model preserves the mean amount, but the other two models tend to reduce the cloudiness under mostly cloudy conditions. This arises from the normalization conditions employed in both models. The first two models also tend to have less variability under almost clear conditions. Variability has a strong impact on the accuracy of the cloud clearing, and the three models produced different accuracies. Although all three models are equally valid, we were interested in assessing the quality of cloud clearing in terms of the tractability of cloud clearing per retrieval set.

We have developed a parameter which most closely indicates when a cloud scene can be cleared. This parameter is an estimate of the uncertainty of the cloud cleared radiances. For known cloud fractions, The measured radiance in an idealized surface channel, e.g. one with zero clear-sky absorption, is a linear combinations of the radiances from surface R_s, and the two cloud layers $R_{\{u,l\}}$. The least squares surface radiance solution has uncertainty

$$\epsilon_{R_s} = \sqrt{\{(\mathbf{F}^T\mathbf{F})^{-1}\}_{R_sR_s}\,\epsilon_R^2}$$

where ϵ_R is the measurement noise and $\mathbf{F}$ is the matrix of viewed cloud and surface amounts

$$\mathbf{F} = \begin{pmatrix} f_{1u} & f_{1l} & 1 - f_{1u} - f_{1l} \\ \vdots & \vdots & \vdots \\ f_{9u} & f_{9l} & 1 - f_{9u} - f_{9l} \end{pmatrix}.$$

Solving for the surface radiance uncertainty must be performed using singular value decomposition because the matrix inversion becomes singular along with the cloud clearing problem. The amount of uncertainty, represented by the amplification of the original radiance noise is the noise amplification factor $\mathrm{NAF} = \epsilon_{R_s}/\epsilon_R$. For a clear retrieval set when all nine footprints are cloud free, NAF is $1/3$ and increases to inf when the cloud clearing problem is singular. Generally, retrieval sets with NAF greater 4 cannot be cloud cleared.

Figure 8 shows the noise amplification factor as a function of model total cloudiness, i.e. $f_u + f_l^{Viewed}$ for the three models (dotted for Model 1, dashed for Model 2 and solid for Model 3). Both the mean NAF (upper curves) and standard deviation of NAF (lower curves) are shown. Model 1 has significantly larger NAF and therefore poorer retrieval results than either of other models, and had greater variability in the amount of NAF for a given amount of total cloudiness. More scenes can be cloud-cleared for the third model when total cloudiness is less than 25%, while the second model had fewer singular cloud scenes for higher amounts of clouds. Model 2 does not produce significant numbers of retrieval sets with total cloudiness greater than 70%, but states having cloudiness greater than 70% have NAF greater than 3 in the other models and produce states which are not not useful for algorithm development.

III. Results

A week of simulated data was created starting on 10 December 2000. We used the operational global aviation forecasts from NCEP and the 1 km composite AVHRR imagery for 11-20 December 1995. The 8 km December 2000 AVHRR data was not suitable because the data during this time was from the AVHRR on the NOAA 14 satellite, NOAA 14 was in a 0430 equator-crossing time orbit then and most of Europe and half of North America and Asia were in darkness when the satellite was overhead. The geophysical states uses the second water vapor model and the second cloud model. For each day, 2,916,000 geophysical states and radiance spectra were generated, grouped into 324,000 retrieval sets. These are divided into 240 six minute granules of 45 scan sets. HSB and AMSU radiances were also simulated and these are discussed in Reference [42].Results of retrieval from these data are discussed in Reference [1].

Figure 9 shows global mean brightness temperatures for the radiance data generated for 15 December 2000. Uncorrelated Gaussian noise has been added to each radiance; the RMS noise is channel-dependent, but otherwise fixed, and is derived from pre-launch calibration data (see Reference [43]).

The channels fall into four major groups, channels with frequencies less than 900 cm^{-1} (group 1) are primarily sensitive to

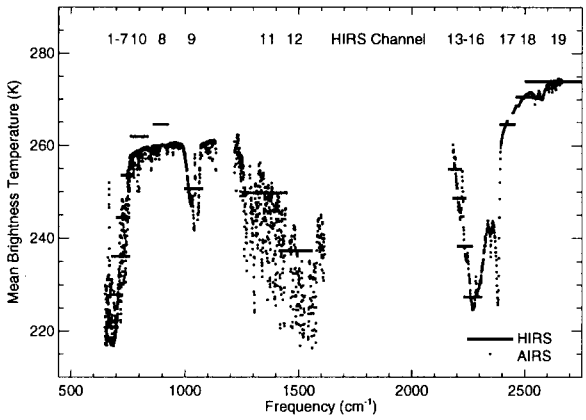

Fig. 9. Average AIRS and HIRS2 Brightness Temperatures

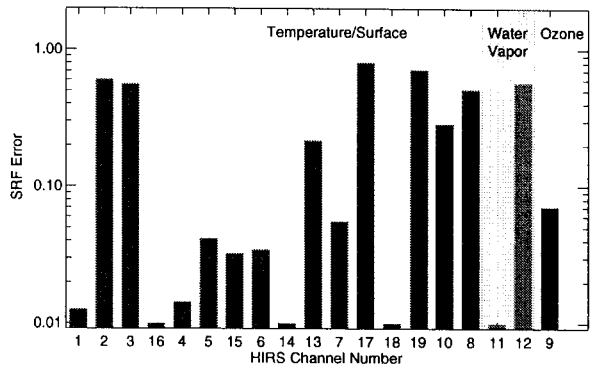

Fig. 10. Error in Fittting AIRS SRF to HIRS2 SRF

emissions from carbon dioxide, but have contributions from the water vapor continuum and the surface; these are used primarily for temperature sounding and cloud clearing. Channels between 900 and 1100 cm^{-1} (group 2) are sensitive to ozone and the surface. The channels between 1200 and 1700 cm^{-1} (group 3) are primarily sensitive to water vapor, and channels greater than 2100 cm^{-1} (group 4) are primarily sensitive to emissions from carbon dioxide and the surface. The radiances in group 4 contain both thermally emitted and solar back-scattered components, but are primarily used for temperature sounding and cloud clearing. In the case of the temperature and ozone sounding groups, channels tend to sound higher in the atmosphere towards the center of the band. Therefore their brightness temperatures decreases through the the troposphere, increases through the stratosphere, and then decreases through the mesosphere towards the center of the band. The decrease associated with the mesosphere is not observed in the ozone bands because of the rapid decrease of ozone mixing ratio above the middle stratosphere. The atmosphere is never opaque for channels in the ozone sensing group and are always sensitive to the surface. Water is an asymmetric rotor with a nearly random distribution of lines. This explains why channels in the water sensing group fluctuate rapidly with frequency, but tend to sense higher in the atmosphere towards 1550 cm^{-1}.

During the chosen week, the High Resolution Infrared Sounder (HIRS2) was operating on the NOAA 14 satellite. NOAA 14 is in a polar orbit very similar to Aqua, but was at an altitude of 800 km and an equator crossing time around 0430. HIRS2 is the infrared sounder currently used for operational weather analysis and forecasting. The HIRS2 scan is similar to AIRS and extends from $\pm 49.5°$, but contains only 56 footprints. The FOV is 1.25°and are separated by 1.8°. HIRS2 scan lines are spaced 42 km between footprint centers. HIRS2 has 19 thermal IR channels, nine in AIRS group 1, one in group 2, two in group 3 and 7 in group 4. The global-mean HIRS2 brightness temperatures are shown in Figure 9 as bars over the channel spectral passband. In each channel, the corresponding AIRS channels show considerable variability. This is because the low spectral resolution of HIRS2 (as compared with AIRS) does not reveal the detailed opacity structure of the atmosphere The AIRS detectors are actively cooled and AIRS signal to noise ratio is comparable to that of HIRS2 even with its higher spectral resolution and shorter integration time (and smaller FOV).

Comparisons between AIRS simulated radiances and actual HIRS2 radiances can be used to assess the realism of the AIRS simulation. Although the two instruments have different spectral resolutions, the AIRS spectral resolution can be averaged to the HIRS resolution. Similarly differences in spatial sampling can be approximated by binning AIRS and HIRS footprints into retrieval sets of comparable size. Lastly, differences in footprint location can be addressed by binning data into a daily fixed spatial grid. Therefore, while HIRS2 and AIRS are very different instruments, it possible to construct comparable data sets.

AIRS radiances can be averaged over many channels to reconstruct the spectral response functions (SRF) of HIRS2. The SRF of HIRS2 channel i, $S_H(\nu, i)$ is represented as a linear combination of AIRS SRF's $S_A(\nu, j)$ with weights $W_{i,j}$.

$$S_H(\nu, i) = \sum_j W_{i,j} S_A(\nu, j)$$

The weights W are found using a least square fit with an uncertainty of

$$\varepsilon_i^2 = \frac{1}{2} \int \{S_H(\nu, i) - \sum_j W_{i,j} S_A(\nu, j)\}^2 \, d\nu \,.$$

The uncertainty is unity when the fit is orthogonal and zero when perfect. Figure 10 shows the fitting error. Channels are ordered by type and location of sensitivity. Channels sensitive to temperature and the surface are shown first, ordered from those that are sensitive to the middle atmosphere (channel 1) through the lower stratosphere and to the surface. Short wave channels are displayed first when multiple channels are sensitive to the same level. The two water channels (11 and 12) are shown next followed by the ozone channel (9). Generally we have not attempted to interpret the water or ozone channels because of the large amount of spectral smoothing indicated by the AIRS data. Eleven HIRS2 channels can be fit by AIRS channels to better than 0.1. The SRF of the other HIRS2 channels extended into gaps in the AIRS spectral bandpass. HIRS2 channels 1, 4, 11, 14, 16 and 18 were particulaly well fit with errors less than 0.02. Even when the HIRS2 SRF's are well fit, there is some uncertainty in the reconstructed radiances because of uncertainty in the HIRS SRF's. The HIRS spectral calibration is not performed under nominal operating conditions and

the SRF depend on ambient temperature. NCEP typically applies radiance bias corrections to HIRS data. The corrections are typically less than 1 K but are as large as -4 K, for channel 15.

Figure 11 shows the mean difference between HIRS2 brightness temperatures and those reconstructed from the simulated AIRS radiances (hereafter referred to as reconstructed). The mean HIRS2 radiances corrected by the NCEP mean bias adjustments are shown by the thick solid line with plus signs. Channel 15, as mentioned previously, is particularly sensitive to SRF uncertainty. After the bias correction, it agrees with channel 6; both channels sees roughly the same level of the atmosphere. Channels 17, 18, 19, 10 and 8 are surface channels. Channels 10 and 8 have sensitivity to water vapor while channels 18 and 19 are sensitive to reflected solar radiance and therefore differences in local solar time. Generally long wavelength tropospheric/surface temperature channels (4,5,6,8,10) are biased warm while short wavelength channels (13-19) are biased slightly cold.

The difference between short and long wavelength channels can be explained by three possible hypotheses, an error in the simulated solar reflected component, an error in the water vapor continuum or an error in the cloud emissivities. An error in cloud amount without a spectral slope in cloud emissivities can not explain the difference. There is a weak trend of increasing negative bias with channel number in the short wavelength channels, but the trend is tied more with the level in the atmosphere where the channels sounds rather than its frequency. This is not consistent with originating from reflected solar radiance. An error in the water continuum could account for some of the error, but there is no evidence that the error decreases away from the water absorption band (channel 10 is worse than 8 which is worse than 12, see Figure 9 for spectral position of HIRS2 channels). On the other hand, the brightness temperature of scenes containing thin cirrus tend to increase with frequency [44],while the simulations assume that the emissivity is uncorrelated with frequency. Because of this, the simulated data does not capture the frequency-dependence of clouds in low sensing channels at the level of around 4 K.

The standard deviation of radiance over the globe is an indication of the amount of variability. The difference between the global standard deviation of HIRS and the reconstructed

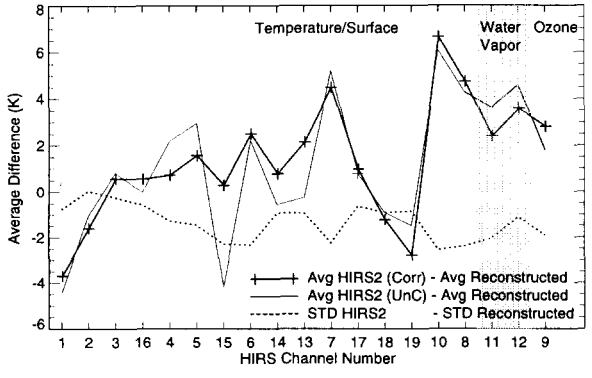

Fig. 11. Mean Difference between HIRS2 and AIRS Brightness Temperatures

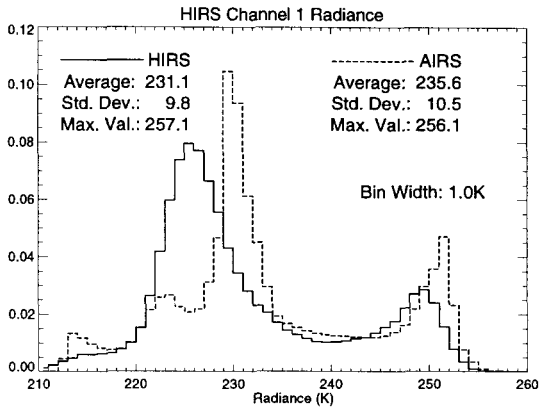

Fig. 12. Comparison between the Density Functions of HIRS2 Channel 1 Brightness Temperatures

brightness temperatures (shown in Figure 11 as a dotted line) is negative when the simulated data have too much variability. Generally the simulated radiances have 1 K of excess variability compared to the total amount around 30 K. Therefore the simulated data does capture the global variability.

Channel 1 senses temperature in the middle atmosphere and shows a -4 K bias. This could impact temperature retrieval in the troposphere and is explored further with Figure 12. Figure 12 shows the density functions of brightness temperature from HIRS2 channel 1, a primary upper middle atmosphere sounding channel. The density function of the reconstructed brightness temperatures (dashed line) and the HIRS2 radiances (solid line) are very similar, but with three differences: the density of reconstructed brightness temperatures has a cold peak at 214 K that is absent in the HIRS2 density, the peak near 230 K in the reconstructed brightness temperature density is narrower and shifted 5 K colder in the HIRS2 brightness temperature density, and the warm peak in the reconstructed brightness temperature density is smaller and 3 K colder in the HIRS2 density. These differences arise because the temperature field on 15 December 2000 was slightly different from the climatology.

The primary sources of variability from climatology are inter-annual variability and planetary wave activity. The latter causes variability around the zonal mean. Planetary waves occur primarily in the winter hemisphere and to a lesser extend as Kelvin waves in the tropics. Figure 13, shows zonal mean brightness temperature and the zonal standard deviation (width of the gray bands) for the HIRS2 data (solid line) and simulated (dashed line). The differences in the warm peak arise from inter-annual variability in the summer hemisphere temperature. The middle peak is associated with tropical regions and the cold peak is associated with polar winter conditions. In the summer hemisphere, the amount of variability in the two fields are roughly equivalent, but the HIRS2 brightness temperatures show greater variability in the tropical and winter hemisphere. This is because the simulated brightness temperatures contains some zonal variability from temperature below 10 hPa, but this is attenuated by the contribution which is provided by climatology. Therefore the differences arise because 1) the middle atmosphere is not climatological on 20 December 2000 and 2) zonal variability in the winter hemisphere is not

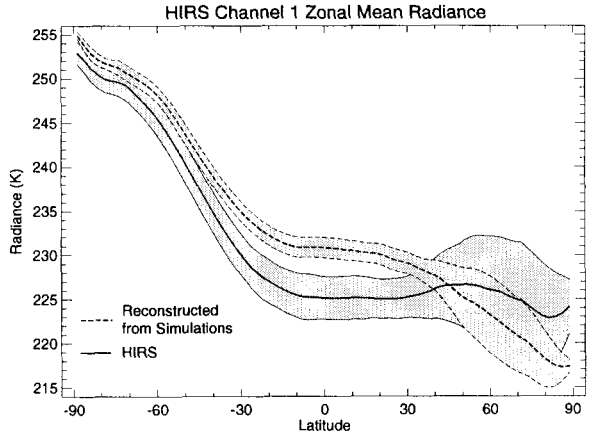

Fig. 13. Zonal Mean HIRS2 Channel 1 Brightness Temperatures

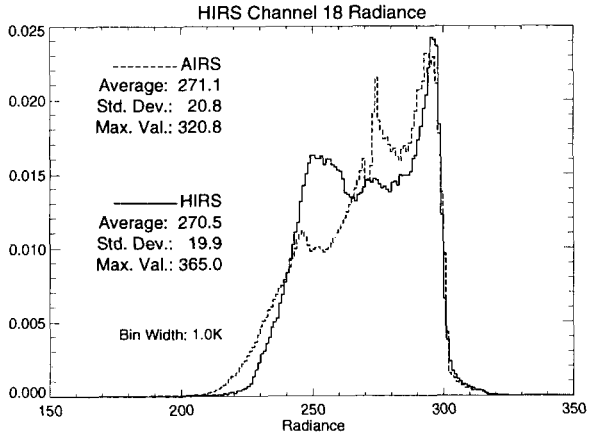

Fig. 14. Histogram of HIRS2 Channel 18 Brightness Temperatures

suitably modeled. Extrapolating back to the simulated AIRS radiances, channels which peak above 10 hPa do not contain sufficient variability to test the retrieval algorithms in the winter. However, this should have minimal effect on troposphere parameters.

Next, a surface channel that is sensitive to clouds throughout the troposphere is examined. Channels that sense the surface and lower troposphere are consistently warmer in the reconstructed radiances. Figure 14 shows the density functions of brightness temperatures for HIRS2 channel 18. Channel 18 is a surface channel that shows a combination of surface emission, cloud emission and solar back-scattering from clouds and the surface. Although the means and standard deviations for the two densities agree to better than 1 K, the densities show many differences. The densities are most similar at the warm end. High brightness temperatures are generally associated with cloud-free footprints. The agreement at this end, indicates that in the absence of clouds, reconstructed radiances are consistent with observations. In both data sets, the highest brightness temperatures occur in the Kalahari desert of Africa, but the simulated brightness temperature can be 45 K smaller than HIRS2. Diurnal variations can not explain the difference, because the HIRS observes Africa at a time when the surface temperature should be cooler than when AIRS makes its measurements. The difference is indicative of limitations of forecast surface model which seem to be pronounced for the dry sands of the Kalahari desert.

Figure 15 is a scatter plot of channel 18 brightness temperature versus latitude. The upper panel shows the reconstructed brightness temperatures, the lower panel are HIRS2 data. The vertical axis is reversed so that brightness temperatures from clear footprints are plotted below cloudy footprints. Similarly, cloudy footprints with high altitude clouds plot above footprints containing low altitude clouds. Partially cloudy footprints plot in between. The warm cloud-free footprints show a similar pattern in both panels with a few differences. The warm footprints near 30° S are more irregular in the HIRS2 data and have larger values; these are from the Kalahari desert of Africa. Generally throughout the southern hemisphere, the fuzziness of the bottom of the scatter shows greater variability in the surface emission in the HIRS2 data. Brightness temperatures at the top of the scatter are associated with footprints which are mostly cloudy or contain high altitude clouds. In the tropics, the HIRS2 data shows many cloudy footprints with brightness temperatures less than 260 K. Many have brightness temperatures close to 200 K corresponding to fully opaque clouds near the tropopause (the tropopause is highest in the tropics and its temperature is typically around 195 to 200 K). This indicates that the simulations do not contain enough equatorial high altitude clouds. Footprints from Antarctica are typically much colder in the simulation. This could arise from excess high altitude cloud or that real polar clouds are more transmissive. The simulation does a remarkable good job of modeling brightness temperatures in mid-latitude, especially in the northern hemisphere. Therefore, while the reconstructed and real HIRS2 radiances have similar statistical properties, regionally, e.g. in the tropics and near the poles, there are differences that could be significant in future uses.

The amount of variability within a retrieval set can be characterized in several ways. We use the standard deviation over the 9 footprints within the set, and calculate the RMS standard deviation over global ensemble of retrieval sets. Figure 16 shows the RMS standard deviation within retrieval sets for the reconstructed radiances (solid line with plus signs). In the middle atmosphere, the local variability is small and grows as the chan-

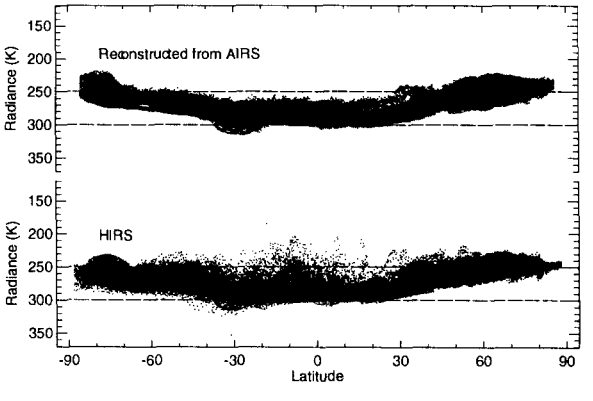

Fig. 15. Zonal Density of Channel 18 Brightness Temperatures

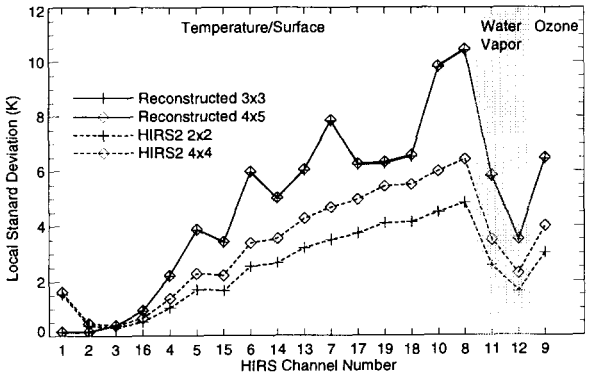

Fig. 16. Local Standard Deviation of AIRS and HIRS2 Brightness Temperatures

nels become more sensitive to clouds and the surface. Short wavelength channels 14, 17, 18 and 19 have slightly less variability than long wavelength channels 7, 8 and 10, even though both sets are sensitive to similar levels (below 600 hPa). This is because the long wavelength surface channels are most sensitive to surface heterogeneity associated with the quartz absorption feature (see Figure 4). In contrast, the short wavelength spectral emissivities of surface materials are relatively flat.

Local variability for the HIRS2 brightness temperatures are also constructed. The HIRS2 scan pattern and NOAA-14 orbit are slightly different from those of AIRS and Aqua. A 2x2 array of HIRS2 footprints is approximately 50 km wide (across track) by 84 km across track at nadir while AIRS retrieval sets at nadir are 42 km by 50 km. However 4x5 arrays of AIRS footprints are 54 km by 85 km and are comparable to HIRS 2x2 arrays. The local variability in HIRS2 2x2 arrays and AIRS reconstructed 4x5 arrays are shown in Figure 16 as the dotted line with plus signs and the solid lines with diamonds. Local variability in HIRS2 4x4 arrays is also shown as a dotted line with diamonds (the difference between 2x2 and 4x4 arrays provides a measure of the dependence on distance).

Local variability on HIRS and AIRS are in good agreement in the stratosphere, but the AIRS data shows increasing more local variability towards the surface, and preferentially in those channels (6,7,8,10) affected by the quartz restrahlen band. Channels 16 and 4 are the lowest channels with surface contributions less than 15% and show some disagreement. This suggests that local variability of cloud amount is slightly over represented in the simulation. Local variability in channels sensing the surface show much greater variability in the simulations. This arises from footprints over land where local variability arises from the varying vegetation. Also, local variability increases with area (2x2 versus 4x4) in the HIRS data, but is independent of size in the simulated data. This lack of spatial correlation arises because the vegetation amount is sampled from the NDVI image rather than averaged over the AIRS FOV. Local variability in the simulation over land derives from the vegetation of 1 km pixels separated by 15 km, hence the absence of correlation.

The primary sources of local variability are clouds and the surface. The simulations slightly overestimates local variability in cloud amount and considerably overestimates surface local variability. The AIRS retrieval algorithms assume that local variability comes just from clouds. Therefore the AIRS simulated data is an overly difficult test of the algorithms. In summary, local variability can be make more realistic by using an averaged NDVI and using cloud model 3 with an effective cloud radius slightly less than 7.5 km.

IV. Conclusions

Simulations provide a tool for developing algorithms, and evolve to serve the needs of development. In the case of these simulations, we started with interpolated forecasts and simple surface and cloud models based entirely on random numbers and gradually added other data sets and more elaborate models. One of the most difficult problems with simulated data is knowing when it is sufficiently realistic. As we collected problematic retrieval sets with common characteristics, we assessed why the retrieval algorithms were unsuccessful. In rare cases we attributed the problem to the simulated data, but we resisted changing the simulation to solve algorithmic problems. Rather we added additional data or developed quasi-physical models that might produce qualitatively different data. In particular, we adopted a physical surface model so that local variability would have realistic horizontal variability. The cloud-models' variability have repeatedly been adjusted to address instability issues we believed would not be present in nature. Cloud-clearing noise amplification factor has been found to be a good indicator of impact on retrieval, and we have presented results for a cloud model which has moderate values of noise amplification factors.

Much later in the development cycle, we began looking at HIRS2 data and identifying methods for validating the simulated data. We have provided evidence that to within a few Kelvin, the simulated brightness temperatures are realistic. Generally the average radiances are biased less than 4 K; simulated radiances are warmer than HIRS2 radiances at long wavelength and colder at short wavelength. We have suggested that this could arise from a wavelength-dependent cloud emissivity or possibly an error in the amount of water vapor. Global variability is generally realistic. The simulated data has 1-2 K more global variability, but this is a small fraction of the total. Local variability is high in the simulated data especially at the surface and the derived retrieved product assessments based on this data are pessimistic.

The data has not addressed realism in vertical correlation or structure within the simulated data because such information is not present in HIRS2 data. Vertical resolution in the model forecasts may be insufficient to resolve 1 km thick features in the atmosphere. Therefore issues concerning the actual vertical resolution of AIRS data will need to be addressed by comparing real data with radiosonde and other high vertical-resolution correlative data after launch.

We expect that simulated data will continue to serve a role in AIRS algorithm development even after launch. It will still provide perfect knowledge about the geophysical state associated with the measurements and will allow us to compare observations with truth both in geophysical parameter and radiance space. Real data will provide the basis for adjusting the simulated data and will provide insight concerning how to interpret

retrievals from simulated data. Lastly since simulated data is derived primarily from forecast, we see an early role for using simulated radiances as part of the validation process and for assessing the additional information AIRS will provide.

ACKNOWLEDGMENTS

E. Fishbein acknowledges the assistance of L. Chen, E. Fetzer, J. Gieselman, B. Lambrigtsen and E. Olsen at JPL in generating and analyzing the simulated data, L. McMillin of NOAA NESDIS for assistance in obtaining calibrated HIRS radiances and M. Goldberg of NOAA NESDIS for suggesting improvements to the surface emissivity simulations. Part of this work was carried out at the Jet Propulsion Laboratory, California Institute of Technology under a contract with the National Aeronautics and Space Administration.

REFERENCES

[1] J. Susskind, C. Barnet, and J. Blaisdell, "Retrieval of atmospheric and surface parameters from AIRS/AMSU/HSB data under cloudy conditions," *IEEE Transactions on Geoscience and Remote Sensing*, submitted this issue.

[2] D. E. Hagan and P. J. Minnett, "AIRS radiance validation over ocean from sea surface temperature measurements," *IEEE Transactions on Geoscience and Remote Sensing*, submitted this issue.

[3] S. Gaiser, H. H. Aumann, and D. Gregorich, "In-flight spectral calibration of the atmospheric infrared sounder," *IEEE Transactions on Geoscience and Remote Sensing*, submitted this issue.

[4] D. Gregorich and H. H. Aumann, "Verification of AIRS boresight accuracy using coastline detection," *IEEE Transactions on Geoscience and Remote Sensing*, submitted this issue.

[5] M. D. Goldberg, L. M. McMillin, W. Wolf, L. Zhou, Y. Qu, and M. Divakarla, "AIRS near real-time products in support of global data assimilation for medium range weather forecasting," *IEEE Transactions on Geoscience and Remote Sensing*, submitted this issue.

[6] H. H. Aumann, M. T. Chahine, C. Gautier, M. Goldberg, E. Kalnay, L. McMillin, H. Revercomb, P. W. Rosenkranz, W. L. Smith, D. Staelin, L. Strow, and J. Susskind, "AIRS/AMSU/HSB on the AQUA mission: Design, science objectives, data products and processing systems," *IEEE Transactions On Geoscience And Remote Sensing*, submitted this issue.

[7] H. H. Aumann and T. J. Pagano, "Atmospheric infrared sounder on the the earth observing system," *Optical Engineering*, vol. 33, no. 3, pp. 776–784, 1994.

[8] G. R. Diak, D. S. Kim, M. S. Whipple, and X. Wu, "Preparing for the AMSU," *Bulletin Of The American Meteorological Society*, vol. 73, no. 12, pp. 1971–1984, 1992.

[9] N. C. Atkinson, "Calibration, monitoring and validation of AMSU-B," *Advances in Space Research*, vol. 28, no. 1, pp. 117–126, 2001.

[10] B. H. Lambrigtsen, "The AIRS microwave instruments: AMSU-A and HSB," *IEEE Transactions On Geoscience And Remote Sensing*, submitted this issue.

[11] C. L. Parkinson and G. Reynold, Eds., *EOS Data Products Handbook*, vol. 2, NASA/Goddard Space Flight Center, Greenbelt, Maryland, 20771, 2000.

[12] G. E. Backus and J. F. Gilbert, "Uniqueness in the inversion of inaccurate gross earth data," *Phil. Tran. Royal Soc. London Sec. A*, vol. 266A, pp. 123–192, 1970.

[13] M. T. Chahine, "Remote sounding of cloudy atmospheres I. the single cloud layer," *J. Atmos. Sci.*, vol. 31, pp. 233–243, 1974.

[14] M. T. Chahine, "Remote sounding of cloudy atmospheres. ii. multiple cloud formations," *J. Atmos. Sci.*, vol. 34, pp. 744–757, 1977.

[15] S. Hannon, L. Strow, S. D. Machado, H. Motteler, and D. Tobin, "An overview of the airs radiative transfer model," *IEEE Transactions on Geoscience and Remote Sensing*, submitted this issue.

[16] P. D. Noerdlinger, "Theoretical basis of the SDP toolkit geolocation package for the ECS project," Tech. Rep. 445-TP-002-002, Hughes Appl. Info. Sys., May 1995.

[17] M. R. Gunson, C. B. Farmer, R. H. Norton, R. Zander, C. P. Rinslandand, J. H. Shawand, and B. C. Gao, "Measurements of CH_4, N_2O, CO, H_2O, and O_3 in the middle atmosphere by the atmospheric trace molecule spectroscopy experiment on spacelab-3," *Journal Geophys. Research*, vol. 95, pp. 13,867–13,882, 1990.

[18] H. L. Pan and L. Mahrt, "Interaction between soil hydrology and boundary-layer development," *Boundary Layer Meteorology*, vol. 38, pp. 185–220, 1987.

[19] J. M. Slingo, "The development and verification of a cloud prediction model for the ECMWF model," *Quart. J. Roy. Meteor. Soc.*, vol. 113, pp. 899–927, 1987.

[20] H. L. Pan and W. S. Wu, "Implementing a mass flux convection parameterization package for the NMC medium-range forecast model," NMC Office Note 409, NOAA/NCEP, NCEP, 5200 Auth Road, Washington, DC 20233, 1995.

[21] NCEP Development Division Staff, "Documentation of the ncep global model," Tech. Rep., NOAA/NCEP Development Division, Washington DC 20233, 1988.

[22] M. Kanamitsu, J. C. Alpert, K. A. Campana, P. M. Caplan, D. G. Deaven, M. Iredell, B. Katz, H. L. Pan, J. Sela, and G. H. White, "Recent changes implemented into the global forecast system at NCEP," *Weather and Forecasting*, vol. 6, pp. 1–12, 1991.

[23] M. Kanamitsu, "Description of the NCEP global data assimilation and forecast system," *Weather and Forecasting*, vol. 4, pp. 334–342, 1989.

[24] J. A. Logan, "An analysis of ozonesonde data for the troposphere: Recommendations for testing 3-d models, and development of a gridded climatology for tropospheric ozone," *Journal of Geophysical Research*, vol. 104, pp. 16,115–16,149, 1998.

[25] J. C. Eidenshink and J. L. Faundeen, "The 1km AVHRR global land data set - 1st stages in implementation," *International Journal of Remote Sensing*, vol. 15, no. 17, pp. 3443–3462, 1994.

[26] D. R. Steinwand, "Mapping raster imagery to the interrupted goode homolosine projection," *International Journal of Remote Sensing*, vol. 15, no. 17, pp. 3463–3471, 1994.

[27] R. J. List, *Smithsonian Meteorological Tables*, Smithsonian Institution Press, Washington, DC, 1958.

[28] C. D. Keelings, R. B. Bacastow, A. F. Carter, S. C. Piper, T. P. Whorf, M. Heimann, W. G. Mook, and H. Roelofzen, "A three-dimensional model of atmospheric CO_2 transport based on observed winds: 1. analysis and observational data.," in *Aspects of Climate Variability in the Pacific and Western Americas*, D. Petersen, Ed., number 55 in Geophysical Series, pp. 165–236. American Geophysical Union, Washington, DC, 1989.

[29] J. M. Wallace and P. V. Hobbs, *Atmospheric Science, An Introductory Survey*, Academic Press, New York, 1977.

[30] K. Masuda, T. Takashima, and Y. Takayama, "Emissivity of pure and sea waters for the model sea-surface in the infrared window regions," *Remote Sensing of Environment*, vol. 24, no. 2, pp. 313–329, 1988.

[31] X. Q. Wu and W. L. Smith, "Emissivity of rough sea surface for 8-13 mu m: Modeling and verification," *applied optics*, vol. 36, no. 12, pp. 2609–2619, 1997.

[32] C. Francois and C. Ottle, "Estimation of the angular variation of the sea- surface emissivity with the ATSR ERS-1 data," *Remote Sensing of Environment*, vol. 48, no. 3, pp. 302–308, 1994.

[33] P. van Delst and X. Wu, "A high resolution infrared sea surface emissivity database for satellite applications," in *Proceedings of 11th International ATOVS Study Conference*, 2000, p. 406.

[34] C. W. Wilber, D. P. Kratz, and S. K. Gupta, "Surface emissivity maps for use in satellite retrievals of longwave radiation," Tech. Rep. TP-19999209362, NASA, 1999.

[35] E. F. Lambin and D. Ehrlich, "The surface temperature-vegetation index space for land cover and land-cover change analysis," *International Journal of Remote Sensing*, vol. 17, no. 3, pp. 463–487, 1996.

[36] T. R. Loveland and A. S. Belward, "The international geosphere biosphere programme data and information system global land cover data set DISCover," *Acta Astronautica*, vol. 41, no. 4-10, pp. 681–689, 1997.

[37] T. Schmugge, S. J. Hook, and C. Coll, "Recovering surface temperature and emissivity from thermal infrared multispectral data," *Remote Sensing of Environment*, vol. 65, no. 2, pp. 121–131, 1998.

[38] R. K. Vincet, *A Thermal Infrared Ratio Imaging Method For Mapping Compositional Variations Among Silicate Rock Types*, Ph.D. thesis, The University of Michigan, 1973.

[39] M. E. Cianciolo, E. O. Schmidt, M. E. Raffensberger, and J. R. Stearns, "Atmospheric scene simulation modeling and visualization," Technical Report PL-TR-96-2079, Phillips Laboratory, Apr 1996.

[40] J. S. Chia Chang, B. Blumberg, G. Anderson, L. Berk, and J. Lee, "Application of MOSART v1.60 and MODTRAN v4.0 for cloud/terrain scene simulation," in *23rd Annual Review of Atmospheric Transmission Models*, Hanscom AFB, Mass., Jun 2000, Air Force Research Lab.

[41] W. Mendenhall, D. D. Wackerly, and R. L. Scheaffer, *Mathematical Statistics with Applications*, PWS Kent, 4th edition, 1990.

[42] E. Fishbein, S.-Y. Lee, and E. Fetzer, "Atmospheric infrared sounder

(AIRS) level 2 simulation system description document," Tech. Rep. Technical Report, Jet Propulsion Laboratory, May 2001, JPL D-20316.

[43] T. S. Pagano, H. H. Aumann, D. E. Hagan, and K. Overoye, "Prelaunch and in-flight radiometric calibration of the atmospheric infrared sounder (AIRS)," *IEEE Transactions on Geoscience and Remote Sensing*, submitted this issue.

[44] E. Schmidt, R. Arduini, B. Wielicki, R. Stone, and S. C. Tzay, "Considerations for modeling thin cirrus effects via brightness temperature differences," *J. Appl. Meteo.*, vol. 34, no. 2, pp. 448–459, 1995.